Journal of Research and Applications in Mechanical Engineering
ISSN: 2229-2152 (Print); 2697-424x (Online)
(2025) Vol. 13, No. 3, Paper No. JRAME 25-13-040
[DOI: 10.14456/ jrame.2025.40]

Research Article

Comparison of High-Order WENO and TENO schemes for Shock Wave Capturing in Compressible-Fluid Simulation

M. Parnichprapa[1]
P. Tunkeaw[2]
W. Rojanaratanangkule[1,*]
[1] *Department of Mechanical Engineering, Faculty of Engineering, Chiang Mai University, Chiang Mai 50200, Thailand*
[2] *Department of Computer Engineering, Faculty of Industrial Technology, Lampang Rajabhat University, Lampang 52100, Thailand*

Received 24 September 2024
Revised 23 December 2024
Accepted 25 December 2024

Abstract:
In this paper, the performance of high-order numerical schemes for capturing small-scale flow structures and shock waves is evaluated. The chosen schemes are a fifth-order WENO scheme of Jiang and Shu (1996) (WENO-JS), a sixth-order WENO with localized dissipative interpolation (CWENO6-CULD) of Wong and Lele (2017), and a sixth-order TENO scheme with adaptive dissipation of Fu, Hu, and Adams (2019). The results indicate that the CWENO6-CULD scheme offers reduced computational time than TENO6-A to 5%, while the TENO6-A scheme excels in capturing both small-scale flow features and shock waves with greater accuracy.

Keywords: *WENO scheme, TENO scheme, Shock wave capturing, Compressible flow, High-order numerical scheme.*

1. Introduction

In computational fluid dynamics (CFD) research, the simulation of compressible flows governed by hyperbolic conservation laws presents a significant challenge, particularly in developing high-order numerical schemes that can both resolve small-scale flow structures and accurately capture discontinuities, such as shock waves. The primary challenge lies in achieving a balance between low numerical dissipation to preserve small-scale flow features and the accurate resolution of discontinuities [1]. In the past, various schemes were developed to address these issues. Harten et al. [2] proposed the ENO scheme, which selects the smoothest sub-stencil to avoid oscillations, while Liu et al. [3] introduced the WENO scheme, which improves accuracy at discontinuities by weighing multiple sub-stencils. Jiang and Shu [4] introduced a smoothness indicator for WENO, leading to the WENO-JS scheme. However, classical WENO schemes face difficulties in achieving fifth-order accuracy at critical points, a problem addressed by Henrick et al. [5] through the WENO-M scheme, which remaps WENO-JS weights to correct for accuracy loss. Borgers et al. [6] followed with the WENO-Z scheme, incorporating a global smoothness indicator to achieve fifth-order accuracy at critical points with computational costs like the WENO-JS scheme. Alternatively, Hu et al. [7] introduced the WENO-CU6 scheme, a sixth-order adaptive central-upwind method incorporating contributions from downwind stencils and adapting between upwind and central schemes depending on the local smoothness. Wong and Lele. [8] introduced CWENO6-CULD scheme. By blending central interpolation with upwind-biased nonlinear interpolation, which is more dissipative, this scheme can resolve complex flow features effectively.

More recently, Fu et al. [9,10,11] introduced a series of high-order TENO schemes aimed at enhancing numerical robustness in comparison to classical WENO schemes. Their research emphasizes the critical role of the cut-off threshold parameter C_T in the TENO weighting process. Nevertheless, standard TENO schemes still face challenges when applying adaptive dissipation. In high-wavenumber regions, minimal dissipation is needed, while in regions with discontinuities, sufficient dissipation is crucial for accurate resolution. Fu et al. [9,10] addressed this with the TENO-A schemes, which adapt the C_T threshold using a near-discontinuity sensor.

* Corresponding author: W. Rojanaratanangkule
E-mail address: watchapon.roj@eng.cmu.ac.th

The objective of this work is to compare six-point stencil WENO and TENO schemes, particularly CWENO6-CULD and TENO6-A, by analyzing their spectral properties using ADR analysis [12]. Various test cases, including linear advection of density and shock-tube problems, are examined.

2. Construction of WENO schemes

The primary numerical challenge is to solve a system of hyperbolic conservation laws that exhibit solutions spanning a wide variety of length scales and discontinuities while maintaining high-order accuracy. To simplify the presentation, the theory is discussed within the framework of a one-dimensional conservation law, written as

$$\frac{\partial u}{\partial t}+\frac{\partial}{\partial x}f(u)=0 \tag{1}$$

In this context, u represents the conservative variable, and f denotes the flux function. The discretization of the problem on a uniform Cartesian grid produces a system of ordinary differential equations, as

$$\frac{du_i}{dt}=-\frac{\partial f}{\partial x}\bigg|_{x=x_i},\ i=0,...,n. \tag{2}$$

where n is the number of grids. Finite-difference scheme can be applied to approximate Eq. (2) as

$$\frac{du_i}{dt}=-\frac{1}{\Delta x}(f_{i+1/2}-f_{i-1/2}) \tag{3}$$

where $f_{i+1/2}$ is fluxes approximated at midpoint by WENO/TENO interpolations.
According to [4], $f_{i+1/2}$ can be reconstructed nonlinearly as

$$\hat{f}_{i+1/2}=\sum_{k=0}^{r-1}\omega_k\hat{f}_{k,i+1/2} \tag{4}$$

Where r is a candidate stencil. For five-point stencils of WENO schemes, The sub-stencils [SL_0 , SL_1 and SL_2], are used while sub-stencils [SL_0 , SL_1 , SL_2 and SL_3] are used for six-point stencils of WENO scheme as shown in Fig. 1.

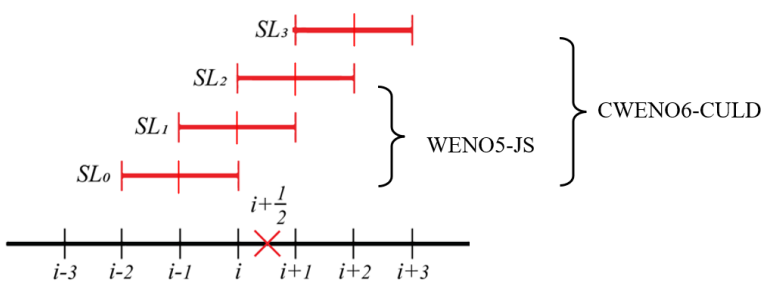

Fig. 1. Five- and Six-point stencils of the WENO5-JS and CWENO6-CULD schemes.

2.1 WENO5-JS scheme

From Eq. (4) the classical fifth-order WENO-JS scheme, the numerical flux approximation at the grid half point $i+1/2$ is represented by

$$\hat{f}_{0,i+1/2}=\frac{1}{6}\left(2f_{i-2}-7f_{i-1}+11f_i\right),$$

$$\hat{f}_{1,i+1/2}=\frac{1}{6}(-f_{i-1}+5f_i+2f_{i+1}),$$

$$\hat{f}_{2,i+1/2} = \frac{1}{6}(2f_i + 5f_{i+1} - f_{i+2}) \tag{5}$$

The nonlinear weight coefficients ω_k are determined by the specific method applied. These weights ω_k are determined by the optimal weights α_k, as

$$\omega_k^{JS} = \frac{\alpha_k^{JS}}{\sum_{k=0}^{2} \alpha_k^{JS}}, \qquad \alpha_k^{JS} = \frac{a_k}{(\beta_k + \varepsilon)^q} \tag{6}$$

In this case, the optimal weights are denoted by $a_0 = 1/10$, $a_1 = 6/10$, $a_2 = 3/10$. The parameter $\varepsilon = 10^{-20}$ is used to prevent division by zero. A cutoff for the smoothness measure is chosen as $q = 2$. The local smoothness indicator β_k is expressed as follows,

$$\beta_k = \sum_{j=1}^{2} \Delta x^{2j-1} \int_{x_{i-1/2}}^{x_{i+1/2}} \left(\frac{d^j}{dx^j} \hat{f}_k(x) \right)^2 dx \tag{7}$$

According to Jiang and Shu [4], the local smoothness indicators are explicitly provided as follows

$$\begin{aligned}
\beta_0 &= \frac{13}{12}(f_{i-2} - 2f_{i-1} + f_i)^2 + \frac{1}{4}(f_{i-2} - 4f_{i-1} + 3f_i)^2, \\
\beta_1 &= \frac{13}{12}(f_{i-1} - 2f_i + f_{i+1})^2 + \frac{1}{4}(f_{i-1} - f_{i+1})^2 \\
\beta_2 &= \frac{13}{12}(f_i - 2f_{i+1} + f_{i+2})^2 + \frac{1}{4}(3f_i - 4f_{i+1} + f_{i+2})^{2,}
\end{aligned} \tag{8}$$

2.2 CWENO6-CULD scheme

The CWENO6-CULD scheme [8,18], features a reconstruction that includes an additional third-order three-point stencil, referred to as $\hat{f}_{3,i+1/2} = \frac{1}{6}(11f_{i+1} - 7f_{i+2} + 2f_{i+3})$. The smoothness indicator β_3 is derived from the complete sixth-point stencil as shown below.

$$\begin{aligned}
\beta_3 = \beta_6 = \frac{1}{120960}[&271779f_{i-2}^2 + f_{i-2}(-2380800f_{i-1} + 4086352f_i - 3462252f_{i+1} + 1458762f_{i+2} - 245620f_{i+3}) \\
&+ f_{i-1}(5653317f_{i-1} - 20427884f_i + 17905032f_{i+1} - 7727988f_{i+2} + 1325006f_{i+3}) \\
&+ f_i(19510972f_i - 35817664f_{i+1} + 15929912f_{i+2} - 2792660f_{i+3}) + f_{i+1}(17195652f_{i+1} \\
&- 15880404f_{i+2} + 2863984f_{i+3}) + f_{i+2}(3824847f_{i+2} - 1429976f_{i+3}) + 139633f_{i+3}^2]
\end{aligned} \tag{9}$$

Due to the implementation of localized dissipative interpolation, two types of nonlinear weights are required. The first type consists of Z-type nonlinear weights for upwind-biased interpolation, ω_k^u while the second consists of C-type nonlinear weights for central interpolation ω_m^c. Since α_3^u is always set to zero, the ω_3^u also becomes zero. The equations for α_k^u and α_m^c are shown below.

$$\begin{aligned}
\omega_k^u &= \frac{\alpha_k^u}{\sum_{k=0}^{3} \alpha_k^u}, \alpha_k^u = a_k \left[1 + \left(\frac{\tau_u}{\beta_k + \varepsilon} \right) \right]^q, k = 0,1,2,3 \\
\omega_m^c &= \frac{\alpha_m^c}{\sum_{m=0}^{3} \alpha_m^c}, \alpha_m^c = b_m \left[C + \left(\frac{\tau_c}{\beta_m + \varepsilon} \right) \right]^q, m = 0,1,2,3
\end{aligned} \tag{10}$$

$\tau_u = |\beta_0 - \beta_2|$ and $\tau_c = |\beta_3 - \beta_{ave}|$ are the fifth and sixth-order reference smoothness indicators, while $\beta_{ave} = (\beta_0 + 6\beta_1 + \beta_2)/8$. To prevent division by zero, the very small value of ε is set to 10^{-20}. In upwind-biased interpolation the parameters $q = 2$ and $a_0 = 1/10$, $a_1 = 6/10$, $a_2 = 3/10$,and $a_3 = 0$ are used, $q = 4$ and $b_0 = 0.05$, $b_1 = 0.45$, $b_2 = 0.45$ and $b_3 = 0.05$ are applied for central interpolation. The process of hybridizing the nonlinear weights begins with calculating the relative reference smoothness indicator, R_τ as

$$R_\tau = \frac{\tau_c}{\beta_{ave} + \varepsilon},$$
$$\omega_k^{CULD} = \begin{cases} \theta\omega_m^u + (1-\theta)\omega_m^c, & if\ R_\tau > 35 \\ \omega_m^c, & otherwise. \end{cases} \tag{11}$$

In this context, ω_m represents the nonlinear weight. The shock sensor θ is in the range of $0 \le \theta \le 1$, that manages the balance between central and upwind-biased interpolations. The value of θ can be obtained from $\theta = max(\theta_i, \theta_{i+1})$ and the sensor is defined as follows

$$\theta_i = \frac{|\Delta f_{i+1/2} - \Delta f_{i-1/2}|}{|\Delta f_{i+1/2}| - |\Delta f_{i-1/2}|} + \varepsilon;\ \Delta f_{i+1/2} = f_{i+1} - f \tag{12}$$

3. Construction of TENO schemes

In contrast to WENO schemes that employ candidate stencils of the same size, TENO schemes implement stencils with progressively increasing widths. For sixth-order TENO schemes, The sub-stencils are [SL_0, SL_1, SL_2 and SL_3] as shown in Fig. 3

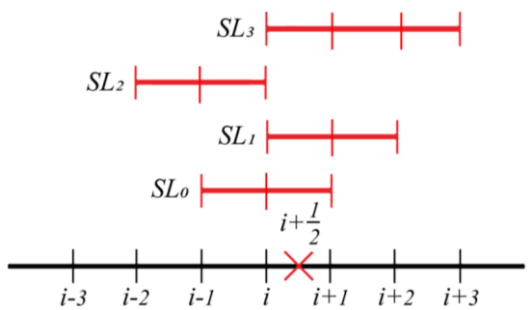

Fig. 2. Six-point stencils of the TENO6-A scheme.

3.1 Six-point TENO Scheme

The candidate fluxes of the 6th -order TENO scheme are computed as follows

$$\hat{f}_{0,i+1/2} = \frac{1}{6}(-f_{i-1} + 5f_i + 2f_{i+1}),$$
$$\hat{f}_{1,i+1/2} = \frac{1}{6}(2f_i + 5f_{i+1} - f_{i+2}),$$
$$\hat{f}_{2,i+1/2} = \frac{1}{6}(2f_{i-2} - 7f_{i-1} + 11f_i),$$
$$\hat{f}_{3,i+1/2} = \frac{1}{12}(3f_i + 13f_{i+1} - 5f_{i+2} + f_{i+3}) \tag{13}$$

According to Fu et al [10], The local smoothness indicators are explicitly given as

$$\begin{aligned}
\beta_{0,3} &= \frac{13}{12}(f_{i-1}-2f_i+f_{i+1})^2+\frac{1}{4}(f_{i-1}-f_{i+1})^2,\\
\beta_{1,3} &= \frac{13}{12}(f_i-2f_{i+1}+f_{i+2})^2+\frac{1}{4}(3f_i-4f_{i+1}+f_{i+2})^2,\\
\beta_{2,3} &= \frac{13}{12}(f_{i-2}-2f_{i-1}+f_i)^2+\frac{1}{4}(f_{i-2}-4f_{i-1}+3f_i)^2,\\
\beta_{3,4} &= \frac{1}{240}[f_i(2107f_i-9402f_{i+1}+7042+f_{i+2}-1854f_{i+3})+f_{i+1}(11003f_{i+1}-17246f_{i+2}+4642f_{i+3})\\
&+f_{i+2}(7043f_{i+2}-3882f_{i+3})+547f_{i+3}^2].
\end{aligned} \tag{14}$$

The smoothness measure is defined as

$$\begin{aligned}
\gamma_k &= \left(C+\frac{\tau_k}{\beta_{k,r_k}+\varepsilon}\right)^q,\\
\tau_k &= \left|\beta_k-\frac{1}{6}(\beta_{1,3}+\beta_{2,3}+4\beta_{0,3})\right|,\\
\chi_k &= \frac{\gamma_k}{\sum_{i=0}^{K-3}\gamma_1},\\
\delta_k &= \begin{cases}0, if\ \chi_k < C_T\\ 1, otherwise\end{cases}.
\end{aligned} \tag{15}$$

The parameter $\varepsilon = 10^{-40}$ serves to avoid division by zero, while $C = 1$ and $q = 6$. The local smoothness of full stencil is represented by β_k , and β_6 can be calculated as shown in Eq. (9). The ENO-like stencil selection strategy relies on measuring smoothness through χ_k. In TENO schemes, stencils identified as non-smooth are discarded or substituted with smooth stencils, which utilize optimal linear weights for reconstruction. The nonlinear adaptation is controlled by a sudden cut-off function and the C_T which remains constant in the classical TENO scheme.

3.2 Adaptive Dissipation Control

The TENO-A (TENO adaptive dissipation control) scheme applies adaptive control of the scheme numerical dissipation in different flow regions. This is achieved by adding a shock sensor to modify the threshold value C_T . For this purpose, an indicator n is introduced as follows

$$\begin{aligned}
n &= 1-min\left(1,\frac{\eta_{i+1/2}}{C_r}\right),\\
\eta_i &= \frac{\left|2\Delta f_{i+1/2}\Delta f_{i-1/2}\right|+\varepsilon}{\left(\Delta f_{i+1/2}\right)^2+\left(\Delta f_{i-1/2}\right)^2+\varepsilon};\varepsilon=\frac{0.9C_r}{1-0.9C_r}\xi^2
\end{aligned} \tag{16}$$

The parameter $\xi = 10^{-3}$ is provided, with $C_r = 0.17$, and $\eta_{i+1/2} = min(\eta_{i-1},\eta_i,\eta_{i+1},\eta_{i+2})$ are applied for six-point reconstruction. The value of C_T is dynamically adapted in response to the local smoothness flow scales. The adaptation strategy for C_T is formulated as

$$\begin{aligned}
g(\mathrm{n}) &= (1-n)^4(1+4n),\\
\overline{\beta} &= \alpha_1-\alpha_2(1-g(\mathrm{n}),\\
C_T &= 10^{-\lfloor\overline{\beta}\rfloor}.
\end{aligned} \tag{17}$$

The Gauss bracket is represented by $\lfloor . \rfloor$ and $g(n)$ is a mapping function based on a smoothing kernel. For six-point reconstruction, $\alpha_1 = 10.5$, and $\alpha_2 = 4.5$ are used. TENO schemes that incorporate adaptive dissipation control are classified as TENO-A. Finaly the nonlinear weight is computed as follows

$$\omega_k^{TENO-A} = \frac{\alpha_k}{\sum_{i=0}^{K-3} \alpha_k}, \alpha_k = a_k \delta_k \tag{18}$$

The optimal weights are $a_0 = 0.4294317718960898$, $a_1 = 0.1727270875843552$, $a_2 = 0.0855682281039113$ and $a_3 = 0.312272912415645$.

The approximated dispersion relation (ADR) analysis [12] is utilized to examine the dispersion and dissipation properties of the different schemes, where ξ_R refers to the real parts (phase error) and ξ_I denotes the imaginary parts (amplitude error) of the modified wavenumber. As shown in Fig. 3, the TENO6-A scheme demonstrates better performance in both dispersion and dissipation compared to the CWENO6-CULD scheme. For central difference schemes of sixth and eighth order, the dissipation properties should be zero.

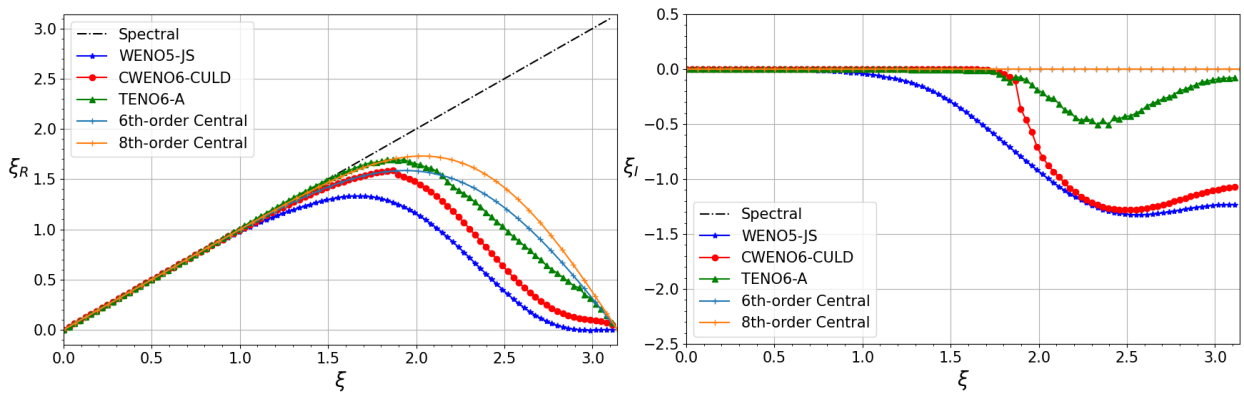

(a) (b)

Fig. 3. (a) Dispersion and (b) dissipation properties of different schemes.

4. Numerical Validation

The following numerical validations illustrate the potential of the WENO5-JS, CWENO6-CULD, and TENO6-A schemes. The flow is governed by the 1D compressible Euler equations. They express the conservation of mass, momentum, and energy as

$$\begin{aligned} &\frac{\partial U}{\partial t} + \frac{\partial f(U)}{\partial x} = 0, \\ &U = \left[\rho, \rho u, E_T\right]^T, \\ &f(U) = \left[\rho u, \rho u u, u E_T\right]^T \end{aligned} \tag{19}$$

where p, u, p *and* E_T are respectively the density, velocity, pressure, and total energy $E_T = p(\gamma - 1) + \frac{1}{2}\rho u^2$.

To close this set of equations, the ideal-gas equation of state $p = (\gamma - 1)\rho e$ with $\gamma = 1.4$ is applied. The convective fluxes are approximated by using the HLLC Riemann solver [18]. The third-order TVD Runge–Kutta [13] is used for time integration.

4.1 Linear advection of density

The numerical accuracy of the chosen schemes is first assessed by examining the one-dimensional Gaussian pulse advection problem [14]. This problem involves solving the linear advection of density equation with an initial condition

$$(p,u,p) = (1+e^{-300(x-x_c)^2},1,1) \tag{20}$$

and the exact solution

$$(p,u,p) = (1+e^{-300(x-t-x_c)^2},1,1) \tag{21}$$

within a computational domain extending from 0 to 1 and $x_c = 0.5$. The final simulation time corresponds to one period ($t = 1$). The uniform grids are employed to analyze the convergence of the L_∞ error. The norm of the error is computed by comparison with the exact solution at the time $t = 1$ according to

$$L_\infty = \max\left|u_i - u_{exact,i}\right| \quad i = 0,...,N_x \tag{22}$$

Grid resolutions of N = 50, 100, 200, 400, 800 and 1600 are selected, while the time step is sufficiently reduced to ensure negligible time integration error. Table 1 presents the statistics for L_∞ error, numerical accuracy order, and CPU time (in seconds). The WENO5-JS, CWENO6-CULD, and TENO6-A schemes achieve fifth, sixth, and fourth-order accuracy, respectively. Additionally, CWENO6-CULD exhibits a lower computational cost than TENO6-A, as indicated by the CPU times.

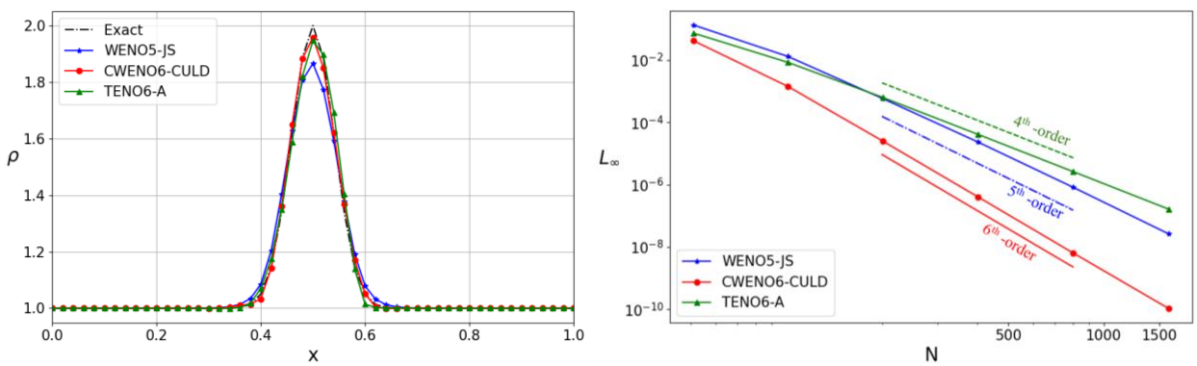

(a) (b)

Fig. 4. (a) Linear advection of density with N=50 and (b) Convergence of the L_∞ error of WENO5-JS, CWENO6-CULD and TENO6-A scheme.

Table 1: L_∞ error, order of numerical accuracy, and CPU time (s) of WENO5-JS, CWENO6-CULD and TENO6-A scheme.

	WENO5-JS			CWENO6-CULD			TENO6-A		
N	L_∞ error	order	CPU time	L_∞ error	order	CPU time	L_∞ error	order	CPU time
50	1.34E-01	*	2.12	4.19E-02	*	2.54	7.38E-02	*	2.74
100	1.32E-02	3.34	6.59	1.44E-03	4.86	8.53	8.53E-03	3.11	9.48
200	5.88E-04	4.49	25.27	2.54E-05	5.83	34.07	6.37E-04	3.74	36.34
400	2.64E-05	4.64	94.63	4.10E-07	5.95	128.76	4.17E-05	3.93	147.61
800	8.27E-07	4.84	450.45	6.44E-09	5.99	549.84	2.63E-06	3.98	616.80
1600	2.65E-8	4.96	1859.26	1.06E-10	5.92	2677.86	1.65E-07	4.00	2745.49

4.2 Sod shock-tube problem

The Sod shock-tube problem [15] is then investigated. The initial conditions used in the test are

$$(\rho,u,p)=\begin{cases}(1,0,1), & if\ x<0\\ (0.125,0,0.1), & if\ x\geq 0\end{cases}, \tag{23}$$

with a computational domain spanning from -0.5 to 0.5, divided into N = 100 uniformly spaced grid points. The simulations are conducted from $t=0$ to $t=0.2$. Fig. 4 presents the computed density distributions, comparing the results obtained using the CWENO6-CULD and TENO6-A schemes. Both schemes demonstrate improved accuracy over the WENO5-JS scheme in resolving the contact discontinuity at locations $x=0.13$ and $x=0.23$. However, concerning the velocity distribution, both CWENO6-CULD and TENO6-A show overshoots at positions $x=-0.03$ and $x=0.02$, indicating a failure to handle the case accurately.

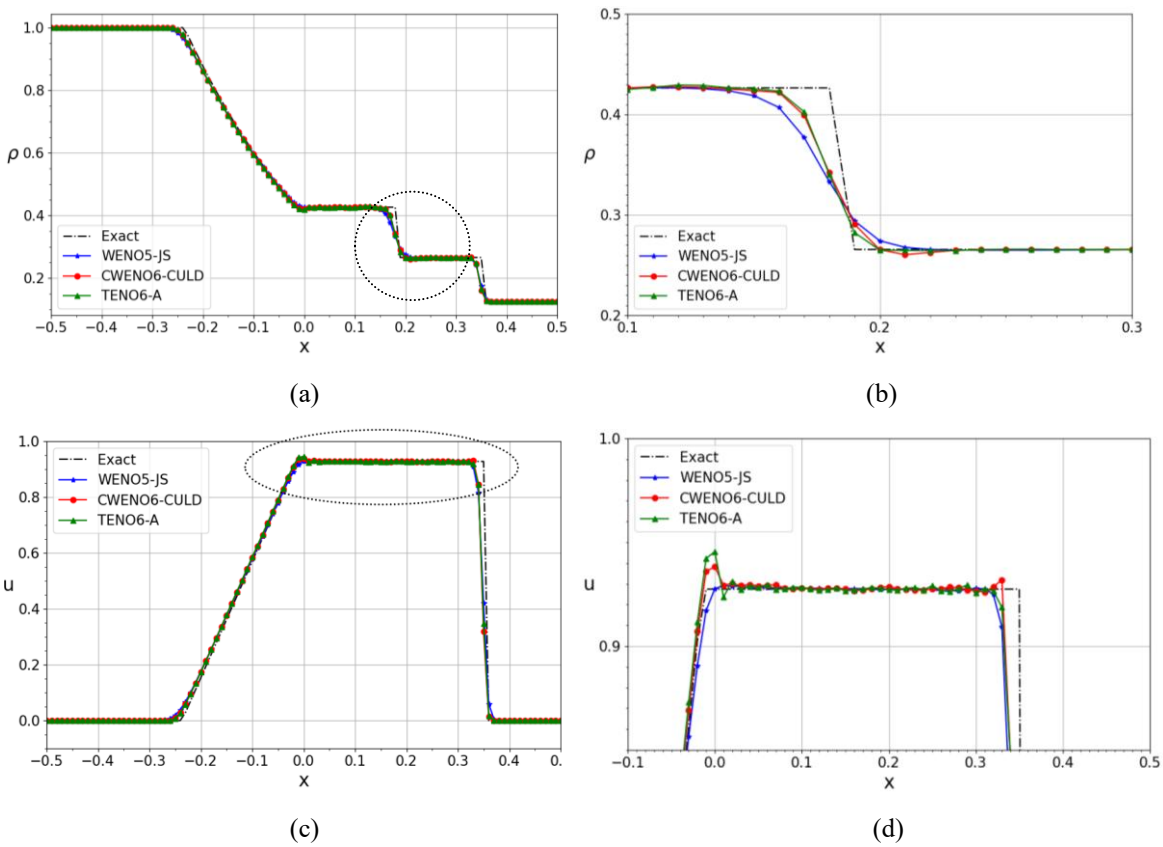

Fig. 5. The Sod shock-tube problem: (a) density distribution and (b) close-up view of near discontinuity; (c) velocity distribution and (d) close-up view of near discontinuity

4.3 Shu–Osher problem

As presented by Shu and Osher [16], the Shu-Osher problem features a Mach 3 shock wave interacting on one-dimensional with a perturbed density field. This interaction generates discontinuities and small-scale structures, making it a challenging benchmark for assessing the effectiveness of numerical schemes in resolving shocks and waves. The initial conditions for the problem are

$$(\rho,u,p)=\begin{cases}(3.857143,2.62936,10.33339), & if\ x<-4\\ (1+0.2sin(5x),0,1), & if\ x\geq -4\end{cases}, \tag{24}$$

with a computational domain from -5.0 to 5.0, discretized into $N = 200$ uniformly spaced grid points. The simulations are conducted from $t = 0$ to $t = 1.8$. The reference exact solution is acquired using the WENO5-JS scheme with a highly refined grid of N=10000 cells,

Fig. 5 shows that CWENO6-CULD and TENO6-A schemes excel at capturing acoustic waves, with TENO6-A demonstrating superior accuracy in maintaining the phase of the density distribution between positions $x = 1$ and $x = 2$. Furthermore, TENO6-A delivers the best resolution for the velocity distribution, particularly preserving amplitude between positions $x = -3$ and $x = -1$.

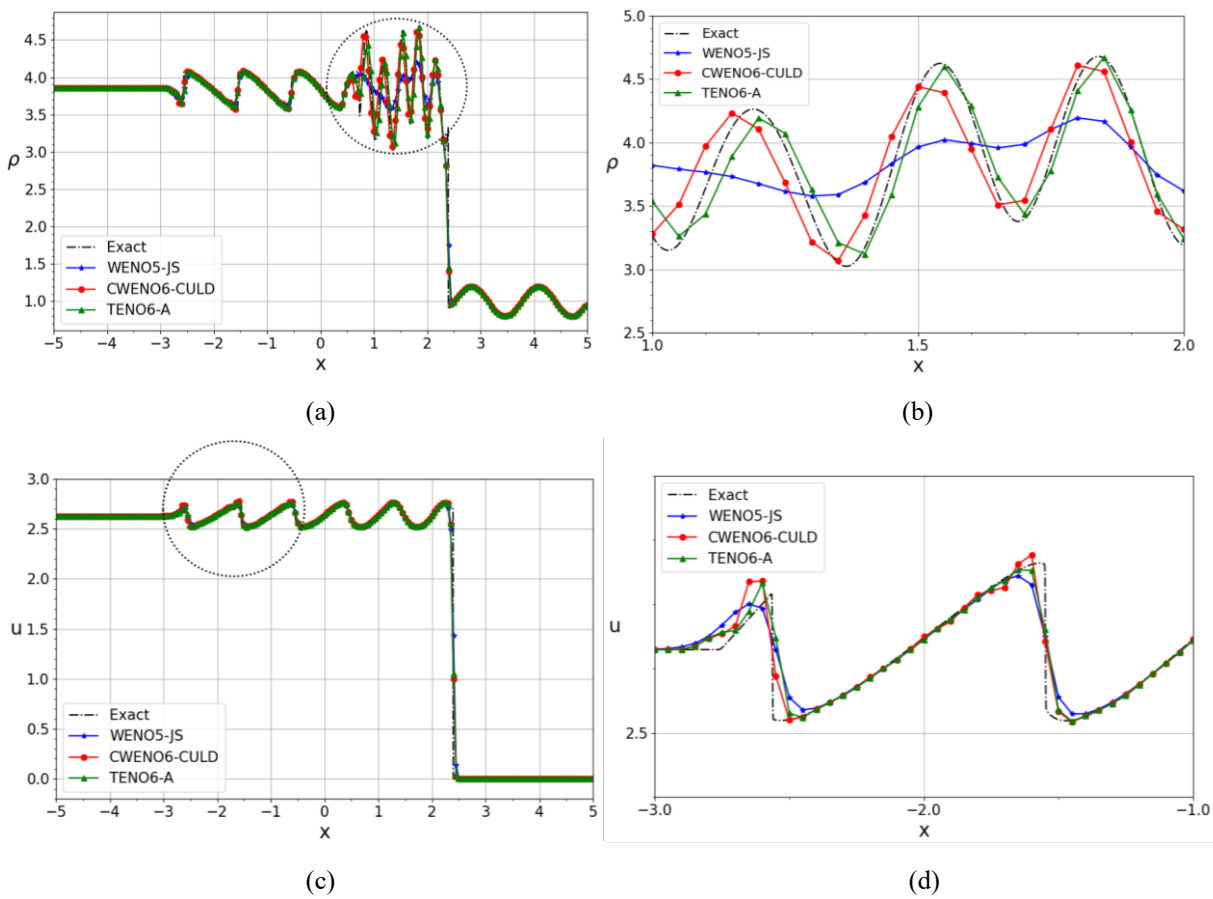

Fig. 6. The Shu-Osher problem: (a) density distribution and (b) close-up view of near wave-resolution; (c) velocity distribution and (d) close-up view of near contact discontinuity

4.4 Titarev–Toro problem

An intensified version of the Shu–Osher problem, the Titarev–Toro problem [17], presents a more severe test of a scheme's shock-capturing capabilities. The initial condition for the Titarev-Toro problem is

$$(\rho, u, p) = \begin{cases} (1.515695, 0.523326, 1.805), & if\ x < -4.5 \\ (1 + 0.1sin(20\pi x), 0, 1), & if\ x \geq -4.5 \end{cases}, \tag{25}$$

The computational domain ranges from -5 to 5 with N = 1000 uniformly spaced grid points. The simulations are conducted from $t = 0$ to $t = 5$. The exact solution is obtained using the WENO5-JS scheme with a highly refined grid of N=10000 cells.

As shown in Fig. 7, in terms of density distributions, the CWENO6-CULD scheme demonstrates superior resolution in preserving both the amplitudes and phase of the density distributions between positions $x=-2$ and $x=-1.5$. Additionally, the CWENO6-CULD scheme significantly outperforms the WENO5-JS and TENO6-A schemes in maintaining the amplitudes and phase of the velocity distributions between positions $x=-1.1$ and $x=-0.6$.

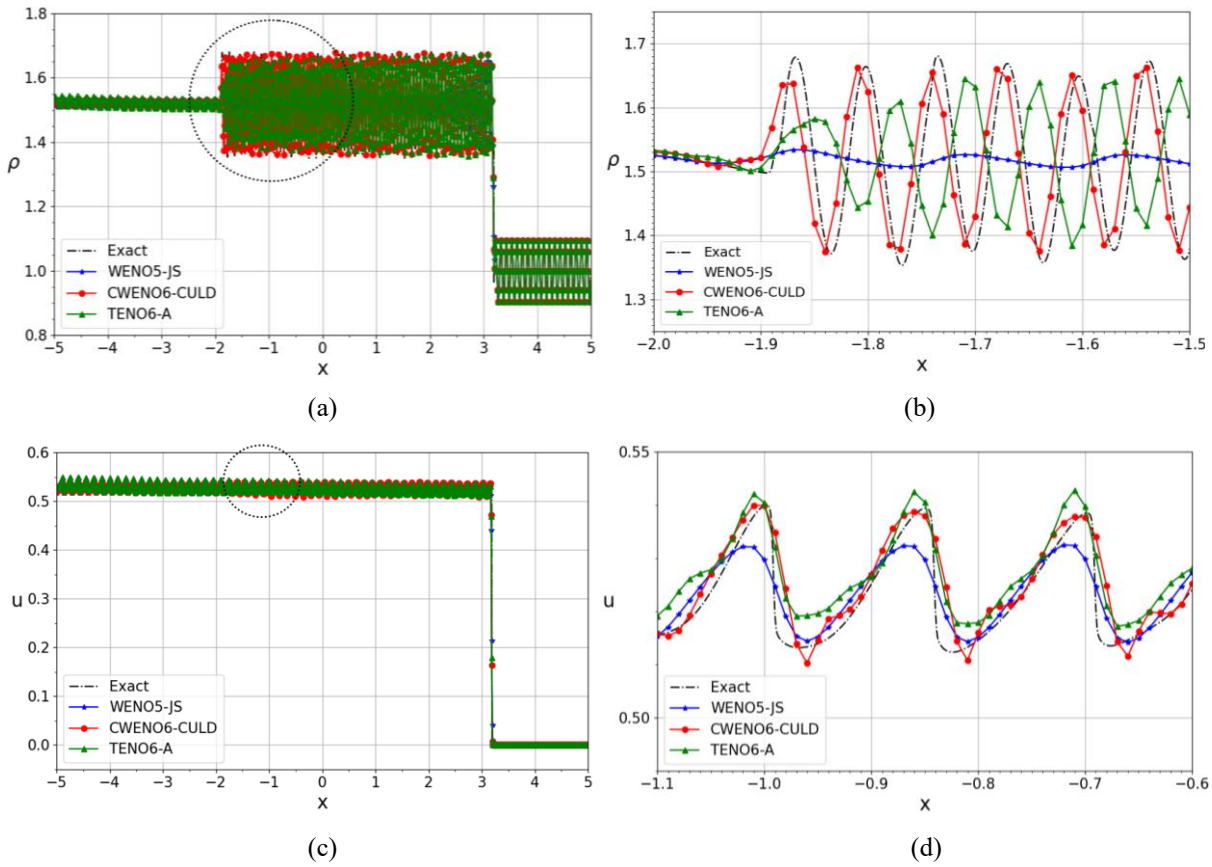

Fig. 7. The Titarev–Toro problem: (a) density distribution and (b) close-up view of near wave-resolution; (c) velocity distribution and (d) close-up view of near contact discontinuity

Fig. 7 presents the density distribution errors for different benchmark tests. The WENO5-JS scheme produced higher errors in the Sod shock-tube and Shu-Osher problems compared to CWENO6-CULD and TENO6-A. However, in the Titarev–Toro problem over the interval $x=-2$ to $x=1$, the TENO6-A scheme showed higher error compared to the WENO5-JS and CWENO6-CULD schemes.

The ρ_{rms} error and CPU time of WENO5-JS, CWENO6-CULD and TENO6-A scheme are summarized in Table 2. The TENO6-A scheme exhibited a lower ρ_{rms} error for both the Sod shock-tube and Shu–Osher problems. The ρ_{rms} error differences between CWENO6-CULD and TENO6-A schemes were 0.00037, 0.03065, and 0.04878, respectively. With respect to CPU time, the CWENO6-CULD scheme demonstrated reduced computational costs across all cases.

Table 2: ρ_{rms} error and CPU time (s) of WENO5-JS, CWENO6-CULD and TENO6-A scheme for benchmark simulations.

	Sod shock-tube		Shu–Osher		Titarev–Toro	
	ρ_{rms} error	CPU time	ρ_{rms} error	CPU time	ρ_{rms} error	CPU time
WENO5-JS	0.01597	7.32	0.16803	16.40	0.07165	84.94
CWENO6-CULD	0.01529	7.61	0.10503	18.06	0.03583	100.44
TENO6-A	0.01492	7.81	0.07438	19.11	0.08461	106.35

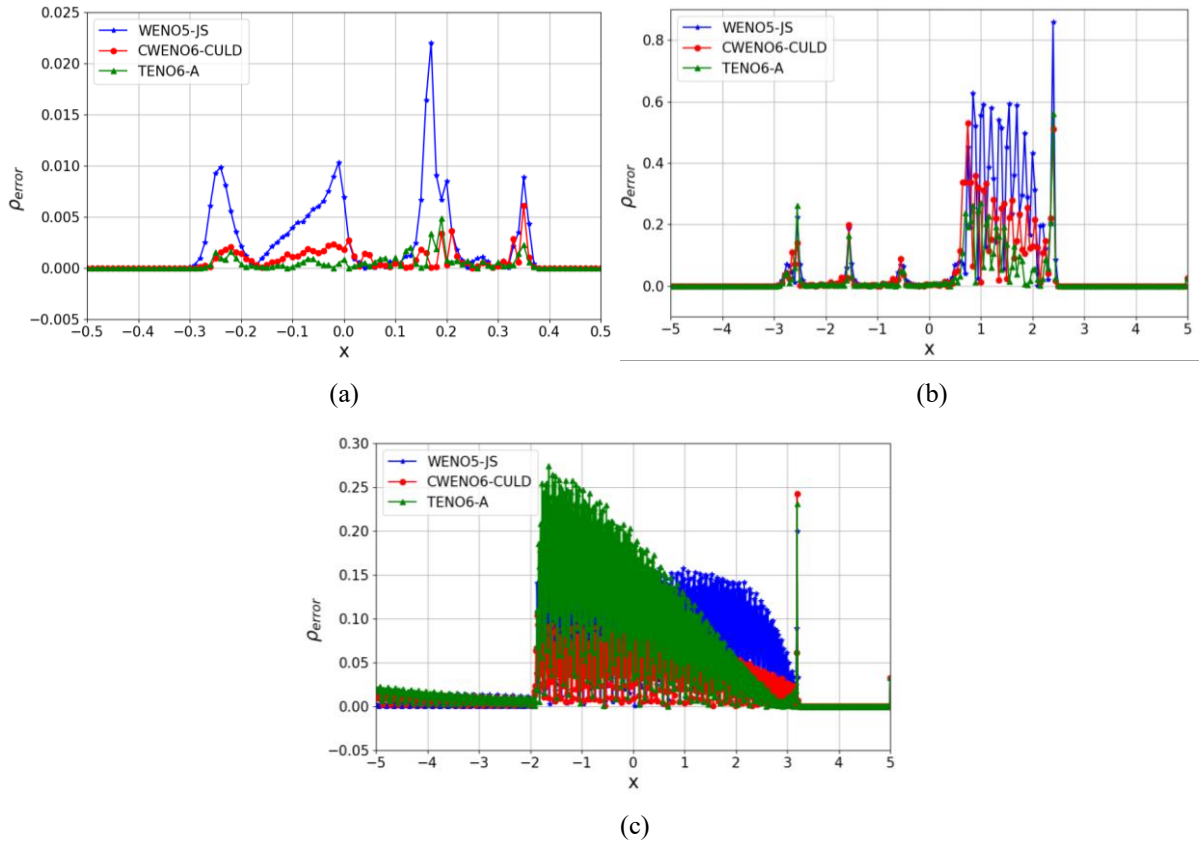

Fig. 8. The ρ error of the various test cases: (a) Sod shock-tube problem, (b) Shu-Osher problem and (c) Titarev–Toro problem

5. Conclusion

This study provides a comprehensive evaluation of the WENO5-JS, CWENO6-CULD, and TENO6-A schemes across several benchmark tests, including linear advection, Sod shock-tube, Shu-Osher, and Titarev-Toro problems. The aim is to assess their capability in capturing small-scale flow structures and shock waves. The results indicate that the TENO6-A scheme exhibits lower numerical dissipation compared to the CWENO6-CULD and WENO5-JS schemes, as demonstrated by the modified wave number analysis. For the linear advection of density test case, the CWENO6-CULD scheme achieves sixth-order of accuracy, surpassing TENO6-A scheme, which achieves fourth-order of accuracy. Across all benchmark tests, the CWENO6-CULD and TENO6-A schemes outperform the WENO5-JS scheme, with CWENO6-CULD scheme offering the added advantage of lower computational cost. However, the TENO6-A scheme excels in capturing small-scale flow structures and resolving shock waves, making it particularly well-suited for high-precision shock-resolution applications. Overall, both WENO and TENO schemes provide significant advantages in applications requiring precise handling of numerical discontinuities and complex flow features, making them essential tools in many fields such as aerospace, automotive engineering, and the simulation of combustion or explosion dynamics.

Nomenclature

$\hat{f}_{i+1/2}$	numerical fluxes
S_r	candidate stencil fluxes
ω_k	nonlinear weighting coefficient
a_k	optimal weights
β_k	The local smoothness indicators
τ_k	The global smoothness indicators
C_T	thresholds constant

Acknowledgement

This research was conducted with the support and resources provided by the Computational Turbulence and Aerodynamics Research Laboratory (CTAR Lab) at Chiang Mai University.

References

[1] Pirozzoli S. Numerical methods for high-speed flows. Annual Review of Fluid Mechanics. 2011;43:163–194.
[2] Harten A, Engquist B, Osher S. Uniformly high order accurate essentially non-oscillatory schemes I. Journal of Computational Physics. 1987;71:231–303.
[3] Liu X-D, Osher S, Chan T. Weighted essentially non-oscillatory schemes. Journal of Computational Physics. 1994;115:200–212.
[4] Jiang G-S, Shu C-W. Efficient implementation of weighted ENO schemes. Journal of Computational Physics. 1996;126:202–228.
[5] Henrick AK, Aslam TD, Powers JM. Mapped weighted essentially non-oscillatory schemes achieving optimal order near critical points. Journal of Computational Physics. 2005;207:542–567.
[6] Borges R, Carmona M, Costa B, Don WS. An improved weighted essentially non-oscillatory scheme for hyperbolic conservation laws. Journal of Computational Physics. 2008;227:3191–3211.
[7] Hu XY, Wang Q, Adams NA. An adaptive central-upwind weighted essentially nonoscillatory scheme. Journal of Computational Physics. 2010;229:8952–8965.
[8] Wong ML, Lele SK. High-order localized dissipation weighted compact nonlinear scheme for shock-and interface-capturing in compressible flows. Journal of Computational Physics. 2017;339:179–209.
[9] Fu L, Hu XY, Adams NA. A family of high-order targeted ENO schemes for compressible-fluid simulations. Journal of Computational Physics. 2016;305:333–359.
[10] Fu L, Hu XY, Adams NA. Improved five-and six-point targeted essentially nonoscillatory schemes with adaptive dissipation. AIAA Journal. 2019;57(3):1143–1158.
[11] Fu L, Hu XY, Adams NA. A targeted ENO scheme as implicit model for turbulent and genuine subgrid scales. Communications in Computational Physics. 2019;26(2):311–345.
[12] Pirozzoli S. On the spectral properties of shock-capturing schemes. Journal of Computational Physics. 2006;219:489–497.
[13] Yamaleev NK, Carpenter MH. A systematic methodology for constructing high-order energy stable WENO schemes. Journal of Computational Physics. 2009;228(11):4248–4272.
[14] Domingues MO, Gomes SM, Roussel O, Schneider K. An adaptive multiresolution scheme with local time stepping for evolutionary PDEs. Journal of Computational Physics. 2008;227:3758–3780.
[15] Sod GA. A survey of several finite difference methods for systems of nonlinear hyperbolic conservation laws. Journal of Computational Physics. 1978;27:1–31.
[16] Shu C, Osher WS. Efficient implementation of essentially nonoscillatory shock-capturing schemes, II. Journal of Computational Physics. 1989;83:32–78.
[17] Titarev VA, Toro EF. Finite-volume WENO schemes for three-dimensional conservation laws. Journal of Computational Physics. 2004;210:238–260.
[18] Tunkeaw J. Direct numerical simulation of compressible two-species mixing layer. Chiang Mai University; 2023.